Complex Analysis of Askaryan Radiation: UHE-ν Identification and Reconstruction via the Hilbert Envelope of Observed Signals

Jordan C. Hanson* and Raymond Hartig

Department of Physics and Astronomy, Whittier College

(Dated: October 2, 2025)

The detection of ultra-high energy neutrinos (UHE-ν), with enegies above 10 PeV, has been a long-time goal in astroparticle physics. Autonomous, radio-frequency (RF) UHE-ν detetectors have been deployed in polar regions. These detectors rely on the Askaryan effect in ice for the neutrino signal. The Askaryan effect occurs when the excess negative charge within a high-energy cascade radiates in a dense medium. UHE-ν can induce such cascades that radiate in the RF bandwidth above thermal backgrounds. To identify UHE-ν signals in data from Askaryan-class detectors, analytic models of the Askaryan electromagnetic field have been created and matched to simulations and laboratory measurements. These models have correctly described the Askaryan electromagnetic field, but leave the effects of attenuation from signal propagation through polar ice and RF channel response to simulation packages. In this work, a fully analytic Askaryan model that accounts for these effects is presented. First, formulas for the observed voltage trace and its Hilbert envelope are calculated. Second, the analytic model is compared to UHE-ν signals at 100 PeV from NuRadioMC, a key Monte Carlo toolset in UHE-ν detection. Correlation coefficients between the analytic signal envelope and MC data in excess of 0.94 are found, and 99.99% of UHE-ν signals pass a correlation threshold of 0.4. Analysis of RF thermal noise reveals that just 0.2 thermal background events pass the correlation threshold in 5 years at a 1 Hz thermal trigger rate. Finally, we present a preliminary reconstruction of the logarithm of the UHE-ν cascade energy from a single string of RF channels.

Keywords: Ultra-high energy neutrino; Askaryan radiation; Mathematical physics

I. INTRODUCTION

Cosmic neutrinos with energies up to 100 PeV have been detected by the IceCube and KM3NeT collaborations [1–8]. Previous analyses indicate that the discovery of UHE-ν flux above 5 PeV requires large Askaryan-class detectors [9]. UHE-ν could reveal the source of ultra-high energy cosmic rays (see sections 3.1-3.3 of [10]). Further, studying electroweak interactions at these energies is impossible on Earth, and Askaryan-class neutrino detectors provide new data (see section 3.4 of [10]).

J. C. Hanson and R. Hartig presented the first fully analytic model of the Askaryan field in the time-domain (HH) [11]. The model builds on earlier work from J. C. Hanson and A. L. Connolly (JCH+AC) for spectral filtering due to coherence effects and the form factor of the instantaneous charge distribution (ICD) [12]. When correlated against semi-analytic parameterizations used in NuRadioMC (ARHZ2020), which involve numeric convolution of UHE-ν cascade data with an analytic vector potential, the HH model yields correlation coefficients in excess of 0.95 [11, 13]. This allows precise reconstruction of UHE-ν cascade parameters, but is limited to comparisons between the simulated and theoretical $\vec{E}$-fields.

Askaryan-class detectors actually observe voltage traces that represent the RF detection channel response, convolved with $\vec{E}$-fields that have propagated through kilometers of polar ice. NuRadioMC accounts for these effects by incorporating measurements from years of lab field work [14–25]. In this work, we present the first fully analytic Askaryan model in the time-domain that matches the observed voltage traces. In practice, it is common to compute the Hilbert envelope of voltage traces from RF channels before cross-correlating them. This is done to remove oscillations introduced by the RF antennas in the channels, which can confuse cross-channel timing and reconstruction. Our calculations include both the voltage trace, and the Hilbert envelope of the trace. The work is organized as follows. Units, definitions, and notational conventions are given in Sec. II. In Sec. III, the calculations of the observed voltage trace and Hilbert envelope of the trace are given. These results are compared to NuRadioMC output in Sec. IV. In Sec. V, the key findings are summarized.

II. UNITS, DEFINITIONS, AND CONVENTIONS

The analysis is based on two analytic functions: the Askaryan signal, $s(t)$, and the RF channel response, $r(t)$. The observed voltage trace in an Askaryan-class detector is $r(t) * s(t)$, the convolution of $r(t)$ and $s(t)$. Let $\hat{s}(t)$ represent the Hilbert transform of $s(t)$, and let $j = \sqrt{-1}$. The *analytic signal* and *signal envelope* are defined by

$$s_a(t) = s(t) + j\hat{s}(t) \tag{1}$$

$$\mathcal{E}_s(t) = |s_a(t)| \tag{2}$$

The signal envelope actually observed by Askaryan-class detectors is the envelope of $r(t) * s(t)$, written as

---

*Electronic address: jhanson2@whittier.edu

Variable	Definition	Units
c	speed of light in medium	m ns^{-1}
r	distance to cascade peak	m
t_r	$t - r/c$	ns
θ_C	Cherenkov angle	radians
θ	viewing angle from cascade axis	radians
a	longitudinal cascade length (see [26])	m
n_{max}	max excess cascade particles (see [26])	none
E_0	$\propto n_{max}a$ (see [26])	V GHz^{-2}
p	$\frac{1}{2}(a/c)^2\left(\cos\theta - \cos\theta_C\right)^2$ (see [11])	ns^2
ω_0	$\sqrt{\frac{2}{3}}(c\sqrt{2\pi}\rho_0)/(\sin\theta)$ (see [12])	GHz
$\sqrt{2\pi}\rho_0$	lateral ICD width (see [12])	m^{-1}

TABLE I: Parameters relevant for Eq. 3.

$\mathcal{E}_{r*s}(t)$. The result for $\mathcal{E}_{r*s}(t)$ depends on the model for $s(t)$, taken to be Eq. 28 in (HH) [11]:

$$r\vec{E}(t_r, \theta) = -\frac{E_0\omega_0\sin(\theta)}{8\pi p}t_r e^{-\frac{t_r^2}{4p} + p\omega_0^2}\,\mathrm{erfc}(\sqrt{p}\omega_0) \quad (3)$$

The parameters of Eq. 3 are shown in Tab. I. Though Ralston and Buniy (RB) [26] used c for the vaccuum value of the speed of light, the formulae for $r\vec{E}$ presented in [26] refer to the wavenumber k in the medium, which is proptional to the index of refraction. Thus, the use of c in this work refers to the speed of light in the medium. For example, a phase factor of $\exp(jkr)$ could also be written $\exp(jr\omega/c)$, if c refers to the value in the medium. The distance r is between the observer and the radiating charge at the cascade peak. The longitudinal length over which $\Delta r < \lambda$, the RF wavelength in ice, is named the *coherence zone* Δz_{coh} in the RB model. The Δz_{coh} is limited by what RB call the "acceleration argument," that $r(t)$ is accelerating while keeping $\Delta r < \lambda$.

The time t is the independent variable of the inverse Fourier transform of the equations in [26]. The delayed time is $t_r = t - r/c$. The speed c is equal to the vacuum value, c_0, divided by the index of refraction n. For the RF bandwidth in solid ice, $n = 1.78$ and $\theta_C = 55.8$ degrees. The viewing angle θ is the zenith angle in spherical coordinates, if the cascade axis is taken to be the z-axis in Cartesian coordinates. The Cherenkov angle is a special zenith angle, $\cos\theta_C = 1/n$ for relativistic cascade particles. The longitudinal cascade length, a, is set by the cascade physics. The ratio $\eta = (a/\Delta z_{coh})^2$ corresponds to the far-field limit as $\eta \to 0$, but this is not a requirement of the RB model. In fact, the RB equations are valid when $\eta > 1$. JCH+AC have shown that η corresponds to low-pass filter with cutoff ω_C that limits the RF emissions, $\eta = \omega/\omega_C$ [12]. JCH+AC also studied ω_C over the frequency and a parameter space, because this parameter space is relevant for the LPM effect.

The n_{max} parameter is the maximum excess negative cascade charge, and the overall RF amplitude, E_0, is proptional to $n_{max}a$ [26]. JCH+AC and HH demon-

strated that the cutoff frequency ω_0 is related to the instantaneous charge distribution (ICD) and the cascade form factor [11, 12]. Monte Carlo simulations have shown that the lateral dependence of the ICD is, to first order, exponentially distributed [12, 27]. JCH+AC derived a closed form for the ICD form factor, $\widetilde{F}(\omega)$, by modeling the lateral component of the ICD as $\exp(-\sqrt{2\pi}\rho_0\rho)$. Finally, HH have shown that the parameter p is related to σ_t, the Gaussian pulse width of $s(t)$ [11]:

$$\sigma_t = \sqrt{2p} \quad (4)$$

The authors of [11] have shown that, because $\cos\theta - \cos\theta_C \approx -\sin\theta_C(\theta - \theta_C)$ to first order in $\Delta\theta = (\theta - \theta_C)$, $p \propto \Delta\theta^2$ to second order, and

$$a\Delta\theta = \frac{c\sigma_t}{\sin\theta_C} \quad (5)$$

Qualitatively, this notion was identified by RB in Sec. III of [26]. HH analyzed the relationship between a, the cascade energy E_C and the critical energy E_{crit} for electromagnetic and hadronic cascades [11]. Let $E_C/E_{crit} = \Lambda$. Assuming the Greisen and Gaisser-Hillas parameterizaions for electromagnetic and hadronic cascades, respectively, HH found the following relationships for the a-values from electromagentically dominated and hadronically dominated cascades:

$$a_{em} = c_{em}\sqrt{\ln\Lambda} \quad (6)$$
$$a_{had} = c_{had}\sqrt{\ln\Lambda} \quad (7)$$

From Eq. 5, the fractional error in $\ln\Lambda$ is:

$$\frac{\sigma_{\ln\Lambda}}{\ln\Lambda} = 2\left(\frac{\sigma_a}{a}\right) \quad (8)$$

Equation 8 corresponds to Eq. 42 in [11], and has been corrected for units. Equations 4-8 imply measurements of a and $\Delta\theta$ yield $\ln\Lambda$, and that the relative error in $\ln\Lambda$ is proportional to the relative error in a.

III. COLLECTION OF MAIN RESULTS

The parameters in Eq. 3 that do not depend on time can be folded into a single constant, E_0, leaving only the essential time-dependence. Let the signal model $s(t)$ be

$$s(t) = -E_0 t e^{-\frac{1}{2}(t/\sigma_t)^2} \quad (9)$$

This is the off-cone field equation from [11]. The parameter σ_t is the pulse width, and it depends two quantities: a and $\Delta\theta$. The parameter E_0 is the amplitude normalization, and the dependencies on other parameters can be determined from Eq. 3 and Tab. I. The Hilbert transform $\widehat{s}(t)$ is equivalent to the convolution of $s(t)$ and the

tempered distribution $h(t) = 1/(\pi t)$. The implication in the Fourier domain is that the negative frequencies in the spectrum of $\hat{s}(t)$ vanish, while the positive ones are doubled. Let the $\text{sgn}(f)$ be -1 if $f < 0$, 0 if $f = 0$, and 1 if $f > 1$, and let $S(f)$ be the Fourier transform of $s(t)$. The Fourier transform $S_a(f)$ of the analytic signal $s_a(t)$ is

$$\mathcal{F}\{s_\text{a}(t)\}_f = S_\text{a}(f) = S(f)(1 + \text{sgn}\, f) \qquad (10)$$

Thus, if $f < 0$, $S_a(f) = 0$, and $S_a(f) = 2S(f)$ if $f \geq 0$. Taking the inverse Fourier transform of Eq. 10, the analytic signal may be written in terms of $S(f)$:

$$s_\text{a}(t) = 2 \int_0^\infty S(f) e^{2\pi j f t} df \qquad (11)$$

The Fourier transform of Eq. 9 is

$$S(f) = E_0 \sigma_t^3 (2\pi)^{3/2} j f e^{-2\pi^2 f^2 \sigma_t^2} \qquad (12)$$

Using the gaussian spectral width σ_f from [12], and the guassian width of $s(t)$ from [11], it was shown in [11] that the uncertainty principle holds for off-cone signals:

$$\sigma_t \sigma_f \geq \frac{1}{2\pi} \qquad (13)$$

The equality is reached in the limit the far-field parameter limits to zero: $\eta \to 0$. This makes the signal spectrum

$$S(f) = E_0 \sigma_t^3 (2\pi)^{3/2} j f e^{-\frac{1}{2}(f/\sigma_f)^2} \qquad (14)$$

Inserting $S(f)$ into Eq. 11, $s_\text{a}(t)$ is

$$s_\text{a}(t) = \frac{E_0 \sigma_t^3 (2\pi)^{3/2}}{\pi} \frac{d}{dt} \int_0^\infty e^{-\frac{1}{2}(f/\sigma_f)^2} e^{2\pi j f t} df \qquad (15)$$

Let $k^2/4 = \frac{1}{2}(f/\sigma_f)^2$, and $x = t/(\sqrt{2}\sigma_t)$. Equation 15 can be broken into real and imaginary parts:

$$s_\text{a}(t) = \frac{E_0 \sigma_\text{t}}{\sqrt{2\pi}} \frac{dI}{dx} \qquad (16)$$

$$\Re\{I\} = \int_0^\infty e^{-k^2/4} \cos(kx) dk \qquad (17)$$

$$\Im\{I\} = \int_0^\infty e^{-k^2/4} \sin(kx) dk \qquad (18)$$

The real part of I is even, so it can be extended to $(-\infty, \infty)$ if it is multiplied by $1/2$. The result is

$$\Re\{I\} = \sqrt{\pi} e^{-x^2} \qquad (19)$$

The imaginary part of I is proportional to the *Dawson function*, $D(x)$ [28]:

$$\Im\{I\} = 2D(x) \qquad (20)$$

The overall analytic signal, $s_a(t)$, is

$$s_a(t) = -E_0 \left(t e^{-\frac{1}{2}(t/\sigma_t)^2} - \frac{2j\sigma_t}{\sqrt{2\pi}} \frac{dD(x)}{dx} \right) \qquad (21)$$

The envelope of the signal, $\mathcal{E}_s(t)$, is the magnitude of Eq. 21. Though $D(x)$ is not evaluated analytically, a high-precision algorithm for computing $D(x)$ was given in [29]. As expected for $\mathcal{E}_s(t)$, $|s_a(0)| \neq 0$, since $dD(x)/dx = 1 - 2xD(x)$. Rather, $|s_a(0)| \propto \sigma_t$.

Observed signals in Askaryan-class detectors is essentially the convolution of the signal and detector response functions. TO generate *signal templates*, signal models are convolved with measured RF channel responses to create *signal templates*. Signal templates are further refined by accounting for frequency-dependent attenuation due to propagation through polar ice [14, 15]. Signal templates are cross-correlated with observed data to identify UHE-ν signals. xxxyyyzzz

Oscillations within signal templates and observed data are often introduced by the RF channel response, and can introduce various uncertainties when cross-correlated. This problem intensifies when the signal-to-noise ratio between Askaryan pulse data and thermal noise decreases. To reduce these uncertainties, the Hilbert envelope of observed signals is used in cross-correlations instead of the original signals. We seek an analytic equation for the Hilbert envelope of the data. That is, we seek the envelope of the convolution of the analytic signal model with a typical detector response. The RLC damped oscillator is a standard circuit model for the RF dipole antennas used in RNO-G and the proposed Ice-Cube Gen2 [10, 30, 31]. There are two paths to calculating the final result. The first option involves three steps. First, the detector response, $r(t)$ is convolved with $s(t)$. Second, the analytic signal of the result is found. Third, the magnitude of the analytic signal is computed, which can be compared to envelopes of observed signals. The second option involves computing the envelope of the convolution of $r(t)$ with $s(t)$ directly from $s_a(t)$ and $r_a(t)$. Let $s(t) * r(t)$ represent the convolution of $s(t)$ and $r(t)$. Let the envelope of the convolution be $\mathcal{E}_{s*r}(t)$. $\mathcal{E}_{s*r}(t)$, $s_a(t)$, and $r_a(t)$ are related by

$$\mathcal{E}_{s*r}(t) = \frac{1}{2}|s_a(t) * r_a(t)| \qquad (22)$$

The proof of Eq. 22 is based on two ideas. First, the Hilbert transform of a function $s(t)$ is equivalent to convolving it with the "tempered distribution" $h(t) = 1/(\pi t)$. Second, computing the Hilbert transform twice yields the original function, multiplied by -1: $h * h * s = -s$. Given the definitions of the analytic signal and the Hilbert transform,

$$(s * r)_a(t) = s * r + j\, \widehat{s * r} \qquad (23)$$

$$\mathcal{E}_{s*r}(t) = |s * r + js * r * h| \qquad (24)$$

However,

$$r_a * s_a = (r + j\hat{r}) * (s + j\hat{s}) \qquad (25)$$

$$r_a * s_a = r * s + jr * \hat{s} + j\hat{r} * s - \hat{r} * \hat{s} \qquad (26)$$

$$r_a * s_a = r * s - r * h * s * h + 2jh * r * s \qquad (27)$$

$$r_a * s_a = r * s - h * h * r * s + 2jh * r * s \qquad (28)$$

$$r_a * s_a = 2r * s + 2jh * r * s \qquad (29)$$

Multiplying both sides $1/2$ and taking the magnitude completes the proof:

$$\frac{1}{2}|r_a * s_a| = |r * s + jh * r * s| = \mathcal{E}_{s*r}(t) \quad (30)$$

Assume that a signal arrives in an RLC damped oscillator at $t = 0$. For $t \geq 0$, the impulse response and corresponding analytic signal are

$$r(t) = R_0 e^{-2\pi\gamma_f t} \cos(2\pi f_0 t) \quad (31)$$
$$r_a(t) = R_0 e^{-2\pi\gamma_f t} e^{2\pi j f_0 t} \quad (32)$$

The parameters γ_f and f_0 are the *decay constant* that corresponds to the *fall time* of the output signal, and the resonance frequency. Note that the envelope of $r(t)$, $|r_a(t)|$, is $R_0 \exp(-2\pi\gamma_f t)$, as expected. To prove Eq. 32, first compute the Fourier transform of $r(t)$:

$$R(f) = \frac{R_0}{4\pi j}\left(\frac{1}{f - z_+} + \frac{1}{1 - z_-}\right) \quad (33)$$
$$z_+ = f_0 + j\gamma_f \quad (34)$$
$$z_- = -f_0 + j\gamma_f \quad (35)$$

Given Eq. 11, the procedure to find $r_a(t)$ is to multiply the *negative* frequency components by 0 and the *positive* frequency components by 2, and take the inverse Fourier transform. The inverse Fourier transform may be completed by extension to the complex plane using the upper infinite semi-circle as a contour, and applying Jordan's lemma. The residue from the pole at z_+ drives the final result. (Check the sign of time here, to ensure that it is positive). The goal is now to apply Eq. 22 by convolving $s_a(t)$ with $r_a(t)$. The calculation may be split into two parts: $r_a(t) * \Re\{s_a(t)\}$, and $r_a(t) * \Im\{s_a(t)\}$. Let $u(t)$ represent the Heaviside step function. Starting with $r_a(t) * \Re\{s_a(t)\}$:

$$r_a(t) * \Re\{s_a(t)\} =$$
$$R_0 e^{2\pi j f_0 t} e^{-2\pi\gamma t} u(t) * \left(-E_0 t e^{-\frac{1}{2}(t/\sigma_t)^2}\right) \quad (36)$$

Let $x = t/(\sqrt{2}\sigma_t)$, $y = \tau/(\sqrt{2}\sigma_t)$, and $z = (2\pi j f_0 - 2\pi\gamma)\sqrt{2}\sigma_t$. Changing variables while accounting for the relationship between $u(t)$, x, and y, gives

$$r_a(t) * \Re\{s_a(t)\} =$$
$$- 2R_0 E_0 \sigma_t^2 \int_{-\infty}^{x} e^{z(x-y)} y e^{-y^2} dy \quad (37)$$

Note that the units for the convolution of $r(t)$ and $s(t)$ correspond to $R_0 E_0 \sigma_t^2$. Let $u = x - y$, so that $du = -dy$. The result is

$$r_a(t) * \Re\{s_a(t)\} = 2R_0 E_0 \sigma_t^2 \left(\frac{dI(x,z)}{dz} - xI(x,z)\right) \quad (38)$$

where

$$I(x,z) = \int_0^\infty e^{zu} e^{-(u-x)^2} du \quad (39)$$

Let $b = x + \frac{1}{2}z$. Completing the square in the exponent and substituting $k = u - b$ gives

$$I(x,z) = e^{-x^2} e^{b^2} \int_{-b}^{\infty} e^{-k^2} dk$$
$$= \frac{\sqrt{\pi}}{2} e^{-x^2} e^{b^2} \operatorname{erfc}(-b) \quad (40)$$

Let $b = jq$, and $w(q)$ be the *Faddeeva function* [28]. The integral becomes

$$I(x,z) = \frac{\sqrt{\pi}}{2} e^{-x^2} w(q) \quad (41)$$

The chain rule is required to find dI/dz:

$$\frac{dI}{dz} = \frac{dI}{dq}\frac{dq}{dz} = -\left(\frac{j}{2}\right)\frac{dI}{dq} \quad (42)$$

The final result is

$$r_a(t) * \Re\{s_a(t)\} =$$
$$- \sqrt{\pi} R_0 E_0 \sigma_t^2 \left(x e^{-x^2} w(q) + \left(\frac{j}{2}\right) e^{-x^2} \frac{dw(q)}{dq}\right) \quad (43)$$

Turning to the convolution of $r_a(t)$ with $\Im(s_a)$,

$$r_a(t) * \Im\{s_a(t)\} =$$
$$\left(R_0 e^{2\pi j f_0 t} e^{-2\pi\gamma t} u(t)\right) * \left(\frac{2E_0 \sigma_t^2}{\sqrt{\pi}} \frac{dD(t/\sqrt{2}\sigma_t)}{dt}\right) \quad (44)$$

Note that $f'(t) * g(t) = f(t) * g'(t) = (f(t) * g(t))'$. Thus,

$$r_a(t) * \Im\{s_a(t)\} =$$
$$\frac{2}{\sqrt{\pi}} R_0 E_0 \sigma_t^2 \frac{d}{dt}\left(e^{2\pi j f_0 t} e^{-2\pi\gamma t} u(t) * D(t/\sqrt{2}\sigma_t)\right) \quad (45)$$

Accounting for the step function in the convolution gives

$$r_a(t) * \Im\{s_a(t)\} =$$
$$\frac{2}{\sqrt{\pi}} R_0 E_0 \sigma_t^2 \frac{d}{dt} \int_{-\infty}^{t} e^{(2\pi j f_0 - 2\pi\gamma)(t-\tau)} D(\tau/\sqrt{2}\sigma_t) d\tau \quad (46)$$

Adopting the earlier definitions of x, y, and z gives

$$r_a(t) * \Im\{s_a(t)\} =$$
$$\frac{2}{\sqrt{\pi}} R_0 E_0 \sigma_t^2 \frac{d}{dx} \int_{-\infty}^{x} e^{z(x-y)} D(y) dy \quad (47)$$

Using the fundamental theorem of calculus, and the limiting cases of $D(x)$,

$$r_a(t) * \Im\{s_a(t)\} =$$
$$\frac{2}{\sqrt{\pi}} R_0 E_0 \sigma_t^2 \left(D(x) + z \int_{-\infty}^{x} e^{z(x-y)} D(y) dy\right) \quad (48)$$

Let $u = x - y$, $z = -k$, and note that $D(x)$ is an odd function. These substitutions give

$$r_a(t) * \Im\{s_a(t)\} =$$
$$\frac{2}{\sqrt{\pi}} R_0 E_0 \sigma_t^2 \left(D(x) + k \int_0^\infty e^{-ku} D(u-x) du \right) \quad (49)$$

The remaining integral is the Laplace transform of the shifted Dawson function, $\mathcal{L}\{D(u-x)\}_k$. The final result is

$$r_a(t) * \Im\{s_a(t)\} = \frac{2}{\sqrt{\pi}} R_0 E_0 \sigma_t^2 \left(D(x) + k\mathcal{L}\{D(u-x)\}_k \right) \quad (50)$$

Though a closed analytic form for $\mathcal{L}\{D(u-x)\}_k$ is elusive, finishing this calculation through numerical integration is straightforward. Combining Eq. 43 and Eq. 50 gives $r_a(t) * s_a(t)$, since

$$r_a(t) * s_a(t) = r_a(t) * \Re\{s_a(t)\} + j r_a(t) * \Im\{s_a(t)\} \quad (51)$$

which yields

$$r_a(t) * s_a(t) =$$
$$- \sqrt{\pi} R_0 E_0 \sigma_t^2 \left(x e^{-x^2} w(q) + \left(\frac{j}{2}\right) e^{-x^2} \frac{dw(q)}{dq} \right) +$$
$$\frac{2j}{\sqrt{\pi}} R_0 E_0 \sigma_t^2 \left(D(x) + k\mathcal{L}\{D(u-x)\}_k \right) \quad (52)$$

The units of convolution should be $R_0 E_0 \sigma_t^2$, and each term in Eq. 52 has these units. Remember that the relationship between q and x is given by

$$q = -jb = -j\left(x + \frac{z}{2}\right) \quad (53)$$

Taking the magnitude of Eq. 52, and multiplying by $1/2$, yields the **Hilbert envelope of the convolution of $s(t)$ with $r(t)$:**

$$\mathcal{E}_{r*s}(t) = \frac{1}{2}|r_a(t) * s_a(t)| \quad (54)$$

It is important to note that the convolution of $s(t)$ and $r(t)$ may be done analytically in the time-domain:

$$s * r = \int_{-\infty}^\infty s(t-\tau) r(\tau) d\tau \quad (55)$$

Inserting the definitions of $s(t)$ and $r(t)$,

$$s * r =$$
$$- E_0 R_0 \int_{-\infty}^\infty (t-\tau) e^{-\frac{1}{2}\left(\frac{t-\tau}{\sigma_t}\right)^2} \Re\left\{e^{2\pi j f_0 \tau} e^{-2\pi\gamma\tau}\right\} u(\tau) d\tau \quad (56)$$

Using the previous definitions of x, y, and z gives

$$s * r = -2R_0 E_0 \sigma_t^2 \int_0^\infty (x-y) e^{-(x-y)^2} \Re\{e^{zy}\} dy \quad (57)$$

Note that the $\Re\{\}$ operator can encompass the whole integral, since $s(t)$ is real. Splitting the integral and employing differentiation under the equals sign yields

$$s * r =$$
$$- 2R_0 E_0 \sigma_t^2 \Re \left\{ x e^{-x^2} I(x,z) - \frac{1}{2} e^{-x^2} \frac{dI(x,z)}{dx} \right\} \quad (58)$$

with

$$I(x,z) = \int_0^\infty e^{-y^2 + (2x+z)y} dy \quad (59)$$

As above, let $b = x + \frac{1}{2}z$, and $b = jq$. In a procedure resembling the calculation for $r_a(t) * \Re\{s_a(t)\}$, the result for $I(x,z)$ is

$$I(x,z) = \frac{\sqrt{\pi}}{2} w(q) \quad (60)$$

where $w(q)$ is the Faddeeva function. Inserting this result into Eq. 58, and distributing the $\Re\{\}$ operator to the instances of $I(x,z)$, gives

$$s * r = -\sqrt{\pi} R_0 E_0 \sigma_t^2$$
$$\Re \left\{ x e^{-x^2} w(q) - \frac{1}{2} e^{-x^2} \frac{dw(q)}{dx} \right\} \quad (61)$$

From the definition of q and the chain rule, $dw(q)/dx = -jdw(q)/dq$, and $dw(q)/dq = -2qw(q) + 2j/\sqrt{\pi}$ [28]. The final result is left in terms of $\Re\{w(q)\}$ and $\Re\{-jdw(q)/dq\}$, which are proportional to the *Voigt functions* [11, 28].

$$s * r = -\sqrt{\pi} R_0 E_0 \sigma_t^2$$
$$\left(x e^{-x^2} \Re\{w(q)\} - \frac{1}{2} e^{-x^2} \Re\left\{ -j\frac{dw(q)}{dq} \right\} \right) \quad (62)$$

To illustrate the accuracy of the model, Eqs. 52-54 and 62, are shown in Fig. 1. To demonstrate that *numerical convolution* of $s(t)$ and $r(t)$ produces the same results as the *mathematical convolution* of $s(t)$ and $r(t)$ (Eq. 62), the corresponding waveforms are shown in Fig. 2.

IV. COMPARISON BETWEEN ANALYTIC CALCULATIONS AND NURADIOMC

- A data set was generated using NuRadioMC for UHE-ν interactions in a cylindrical ice volume (see Tab. II). The 100 PeV interactions included charged and neutral electroweak currents, and the LPM effect. The Askaryan model used to generate the UHE-ν signals was ARZ2020 [13]. ARZ2020 is a semi-analytic parameterization of the Askaryan effect, in which a vector potential $\vec{A}(\vec{r}, t)$ is convolved with the profile of the charged particle cascade caused by the UHE-ν interaction. ARZ2020
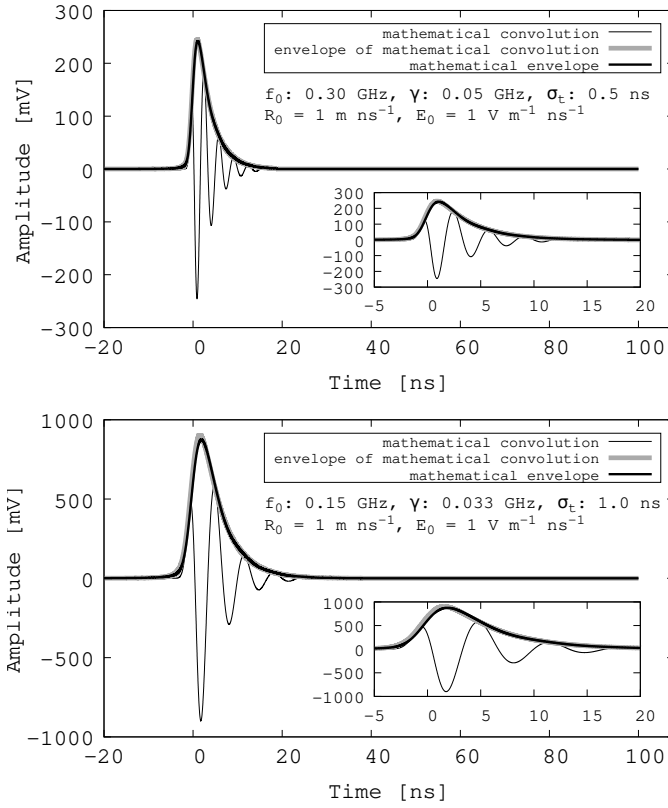
FIG. 1: (Top) The thin black line represents $s(t) * r(t)$. The light gray envelope represents the envelope of $s(t) * r(t)$ computed with the Python3 SciPy function scipy.special.hilbert. The dark gray envelope represents Eq. 52-54. (Bottom) Same as top, for different parameter values.

FIG. 2: (Top) The thin black line represents $s(t) * r(t)$, produced using the Python3 SciPy function scipy.signal.convolve. The dark gray line represents Eq. 62. (Bottom) Same as top, for different parameter values.

accounts for sub-cascades and the LPM effect, and it has been validated against MC simulations [27, 32]. The Askaryan signal model used in NuRadioMC for this analysis was *not* HH2022 [11]. Thus, the correlation between MC output (ARZ2020) and Eqs. 52-54 (HH2022 and this work) is physical.

The detector was *a single string* of 8 RF dipoles. The ice volume had a depth and radius of 0.65 km and 0.85 km, respectively, and the dielectric properties of the South Pole. Each RF channel had a filtered, amplified passband of [0.08-1] GHz, and 256 samples at a 1 GHz sampling rate. The RF trigger responded when any 3 of the 8 voltage traces exceeded $\pm 3 v_{\mathrm{rms}}$ of the thermal noise (233K) within a 256 ns window. The Hilbert envelope of the coherently summed waveform (CSW) was calculated from the traces and correlated against Eqs. 52-54. Each correlation was maximized by varying σ_t. A rough optimization over a noiseless data set yielded 0.15 GHz and 0.025 GHz for the f_0 and γ parameters, respectively. For each signal, a separate thermal noise trace satisfying the RF trigger was generated and correlated against the best-fit
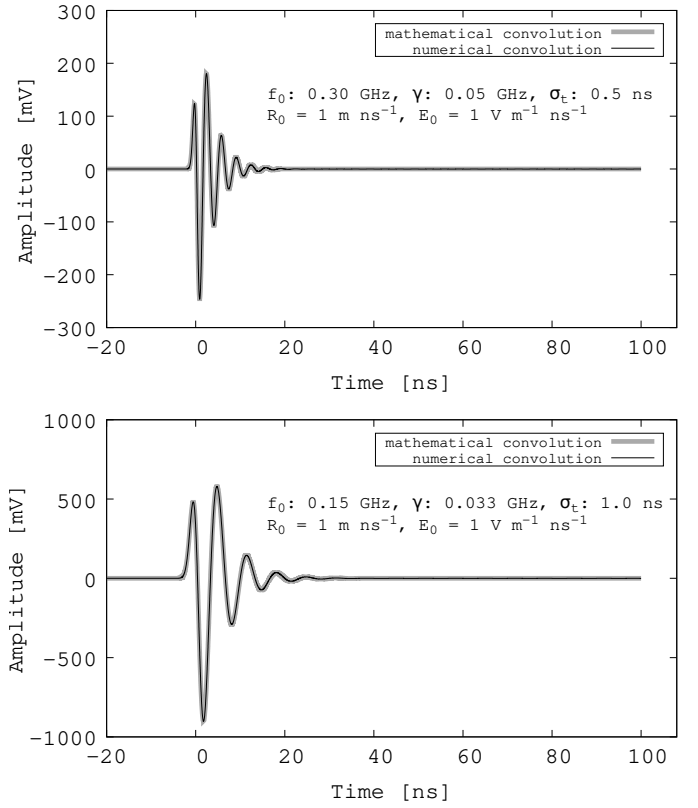
Parameter	Value	Note
Ice Model	South Pole	2015 measurements
Signal Model	ARZ2020	(see [13])
Trigger	3 of 8 channels	high-low trigger at $3v_{\mathrm{rms}}$
RF channels	8	RF bicone (in firn)
Noise Temperature	233K	
Sampling Rate	1 GHz	
Samples per channel	256	
Channel depths	[-4,-6,-8,...-18] m	cable delays included
RF cable type	LMR-400	

TABLE II: Important NuRadioMC parameters used in this analysis.

analytic envelope. The results are shown in Fig. 3.

In Fig. 3, the circles represent the normalized histogram of the correlation coefficent between the optimized analytic envelope and thermal noise. A fitting function of the form $x^2 \exp(-0.5x^2)$ was fit to the noise distribution, and is represented by the gray dashed line. The solid gray line represents the signal distribution, which peaks at a correlation value of 0.94. Lower signal correlation values correspond to lower SNR values (Fig. 4). The verti-
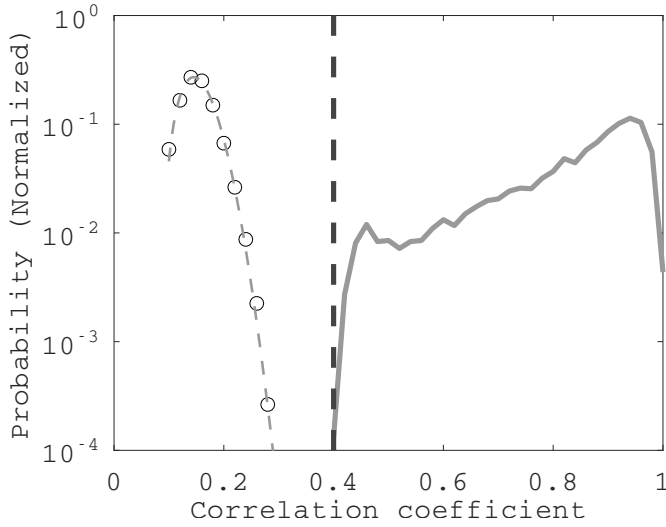
FIG. 3: (Black circles) Noise distribution. (Gray dashed line) Fitting function to noise distribution. (Solid gray line) UHE-ν signal distribution. (Dashed black line) Optimized correlation coefficient threshold value.
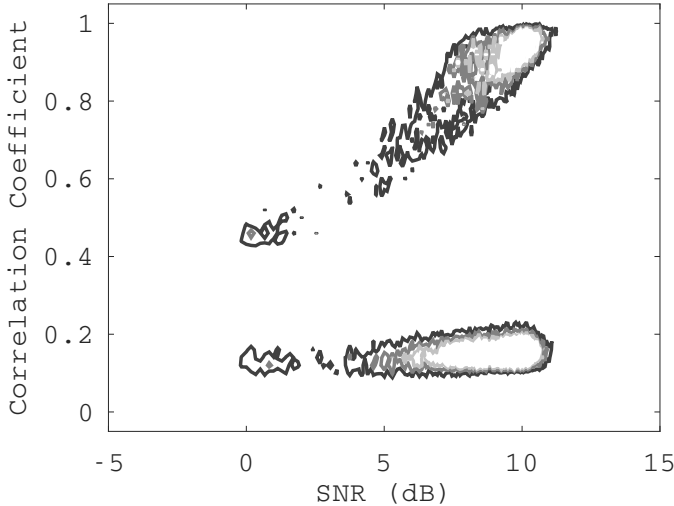

FIG. 4: The correlation versus SNR (dB) for UHE-ν signals (upper distribution) and RF thermal noise (lower distribution). Color scale: normalized histogram value, with five equally spaced contours between 0.0 and 0.002.

cal black dashed line represents a threshold of 0.4. For the simulated UHE-ν, 99.99% of correlations between CSWs and analytic envelopes are greater than or equal to this threshold. Assuming a thermal trigger rate of 1 Hz, integrating the PDF of the noise distribution above the correlation threshold is equivalent to 0.2 noise events every 5 years. An example CSW fit by the analytic envelope is shown in Fig. 5.

The correlation between the optimized analytical envelope and UHE-ν signals depends on the signal
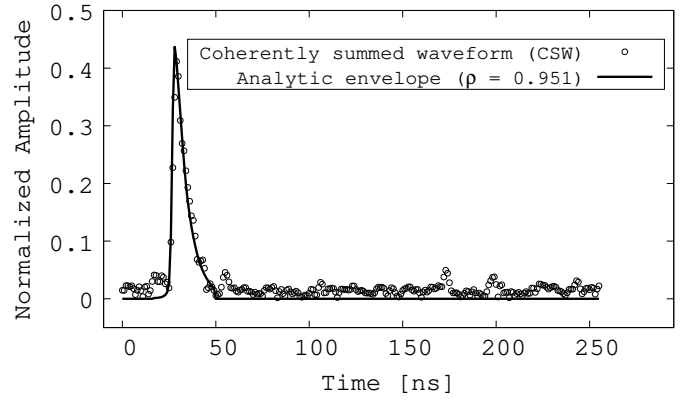

FIG. 5: A single-pulse CSW signal (black dots) from a 100 PeV UHE-ν, matched to an analytic envelope (thick black line) with a correlation coefficient $\rho = 0.951$.

to noise ratio (SNR). Let v_{pp} and v_{rms} represent the peak-to-peak and rms values a voltage traces, respectively. The SNR, in decibels, is defined as

$$\mathrm{SNR}_{\mathrm{dB}} = 20 \log_{10} \left(\frac{1}{2} \frac{v_{\mathrm{pp}}}{v_{\mathrm{rms}}} \right) \qquad (63)$$

In Fig. 4, the correlation coefficient is plotted versus the SNR in dB for the data shown in Fig. 3. The upper and lower distributions correspond to CSWs from UHE-ν events and thermal noise, respectively. All RF thermal noise events satisfy the station trigger ($\pm 3 v_{\mathrm{rms}}$ HL threshold). The correlation coefficient for UHE-ν events is proportional to $\mathrm{SNR}_{\mathrm{dB}}$, while the correlation coefficient for thermal noise is independent of $\mathrm{SNR}_{\mathrm{dB}}$. Note that the SNR of a CSW does not equal the SNR of the individual voltage traces. Rather, the individual voltage traces will have SNR values approximately 5-10 dB *lower* than the CSW SNR. If N voltage traces contain signal, computing the CSW raises the linear SNR by a factor of $\sqrt{N}$, and adds to the SNR in dB a factor of $20 \log_{10}(N)$. For an event with 3 of 8 channels containing signal, $20 \log_{10}(3) \approx 5$ dB, while $20 \log_{10}(8) \approx 9$ dB. The exact increase depends on how many RF channels contain signal.

• Equations 5-8 may be used to reconstruct the natural logarithm of the UHE-ν cascade energy, $\ln \Lambda$. For Eq. 5, σ_t is measured from the optimized analytic envelope, c and θ_C are known constants, and an assumption must be made for $\Delta\theta$. We will make the assumption that $\Delta\theta \approx \Delta\theta_{\mathrm{rms}}$. The assumption is justified since the $\Delta\theta$ distribution is Gaussian. The MC truth for $\Delta\theta$ in this analysis is shown in Fig. 6, with a Gaussian fit ($\mu = -1.05$ deg, $\sigma = 3.02$ deg). The rms and the σ parameter are equal for Gaussian distributions with zero mean, so we let $\Delta\theta \rightarrow \Delta\theta_{\mathrm{rms}}$. The fractional error $\sigma_{\Delta\theta}/\Delta\theta$
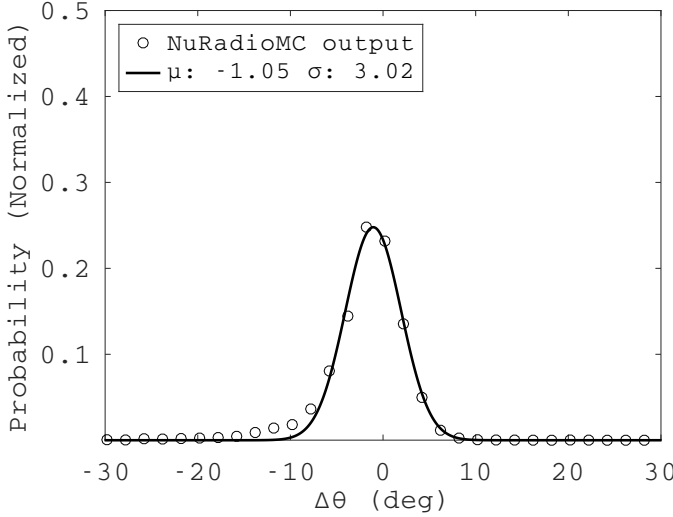
FIG. 6: (Black circles) Viewing angle from NuRadioMC. (Solid black line) Gaussian fit, with $\mu = -1.05$ deg, and $\sigma = 3.02$ deg. (Black dashed line) Cherenkov angle, θ_{C}.

is then set to 1.0, reflecting uncertainty in this parameter. Solving Eq. 5 for a gives

$$a = \frac{c\sigma_t}{\Delta\theta_{\mathrm{rms}}\sin\theta_{\mathrm{C}}} \tag{64}$$

The result for the fractional error in a is found by propagating error from σ_t and $\Delta\theta$, defined as ϵ and $\sigma_{\Delta\theta}$, respectively. The result is

$$\frac{\sigma_a}{a} = \left(\left(\frac{\epsilon}{\sigma_t}\right)^2 + \left(\frac{\sigma_{\Delta\theta}}{\Delta\theta}\right)^2 \right)^{1/2} \tag{65}$$

The first term is small compared to the second, as it is limited by the scan resolution for σ_t and the number of samples per analytic envelope. The scan resolution is set to 0.2 ns in the optimization, and there are typically > 10 samples per envelope, or about 10 ns. Thus, $(\epsilon/\sigma_t)^2$ is two orders of magnitude smaller than $(\sigma_{\Delta\theta}/\Delta\theta)^2$, so

$$\frac{\sigma_a}{a} = \left|\frac{\sigma_{\Delta\theta}}{\Delta\theta}\right| = \left|\frac{\Delta\theta_{\mathrm{rms}}}{\Delta\theta_{\mathrm{rms}}}\right| \approx 1 \tag{66}$$

Setting the ratio to 1 reflects the idea that the rms is equal to σ for a normal distribution. Inserting this assumption into Eq. 8 gives

$$\frac{\sigma_{\ln\Lambda}}{\ln\Lambda} \approx 2 \tag{67}$$

Using Eqs. 6 and 7, the logarithm of the energy is

$$\ln\Lambda = \left(\frac{c\sigma_t}{c_{\mathrm{em/had}}\Delta\theta_{\mathrm{rms}}\sin\theta_{\mathrm{C}}}\right)^2 \tag{68}$$

Using Eqs. 10 and 12 from HH2022 ([11]), c_{em} and c_{had} were found to be 0.80 and 0.93 meters, respectively (FWHM, $R = 0.5$). Using Eq. 68, the σ_t results from the optimized envelope fits to UHE-ν signal CSWs may be used to deduce the logarithm of the UHE-ν cascade, $\log_{10} E_{\mathrm{C}}$. First, converting to the base-10 logarithm introduces a factor of $\ln(10)$ in the denominator of Eq. 68. Second, $\ln\Lambda = \ln(E_{\mathrm{C}}/E_{\mathrm{crit}})$, where E_{C} is the cascade energy, and $E_{\mathrm{crit}} \approx 10^8$ eV is known as the critical energy [11]. Since $\ln\Lambda = \ln E_{\mathrm{C}} - \ln E_{\mathrm{crit}}$, separating this ratio adds a constant to the right hand side of Eq. 68. Third, let c_{ave} be the average of c_{em} and c_{had}, reflecting the unknown hadronic or electromagnetic nature of the cascade. The modified form of Eq. 68 is

$$\log_{10} E_{\mathrm{C}} = \frac{(c\sigma_t)^2}{\ln 10(c_{\mathrm{ave}}\Delta\theta_{\mathrm{rms}}\sin\theta_{\mathrm{C}})^2} + \log_{10} E_{\mathrm{crit}} \tag{69}$$

Table III contains the preliminary results for the reconstruction of $\log_{10} E_{\mathrm{C}}$. The results are consistent with the MC truth. Note that when applying the change of base formula, factors of $\ln(10)$ cancel in the error ratio of Eq. 67, so the error in $\log_{10} E_{\mathrm{C}}$ remains 2.0. The σ_t result is the average value of optimized analytic envelopes fit to signal CSWs generated by 15133 UHE-ν events that triggered the detector with $E_{\mathrm{C}} = 100$ PeV. Note that the error in the *average* σ_t over all events fluctuates due to varying $\Delta\theta$, while the error in *individual* σ_t per CSW fit is negligible if the samples per CSW is much greater than 1. By far, the largest sources of systematic error are *reflected signals* in the CSWs.

Reflected signals are caused when more than one ray-tracing solution is available between the Askaryan radiation source and the detector. Signals that propagate directly to the detector are known as *direct signals*, while signals that first reflect at the snow-air interface, or in the glacial firn, are known as *reflected signals*. Complex RF signal propagation in polar ice has been studied, and even proposed as a UHE-ν energy reconstruction technique [21, 33]. When *direct* and *reflected* signals both arrive at the detector, recorded voltage traces contain both direct and reflected signals. The analytic envelope, however, assumes a single pulse. Thus, direct and reflected pulses that overlap, or are closely spaced, yield larger σ_t values than the average quoted in Tab. III. This effect systematically overestimates the $\log_{10} E_{\mathrm{C}}$. An example of a CSW event with direct and reflected components fit by an analytic envelope is shown in Fig. 7.

Parameter	Average Value
MC Truth, $E_{\rm C}$ [eV]	10^{17}
MC Truth, $\log_{10} E_{\rm C}$	17
c	$0.3/1.78$ m ns^{-1}
$\overline{\sigma_t}$	1.229 ± 0.004 ns
$c_{\rm ave}$	0.86 m
$\Delta\theta_{\rm rms}$	3.78 ± 0.04 degrees
$E_{\rm crit}$	100 MeV
$\sin\theta_{\rm C}$	0.8271
Reconstructed $\log_{10} \mathbf{E_C}$	16.5 ± 2.0

TABLE III: Energy reconstruction parameters used to calculate the logarithm of the UHE-ν cascade energy, $\log_{10} E_{\rm C}$.
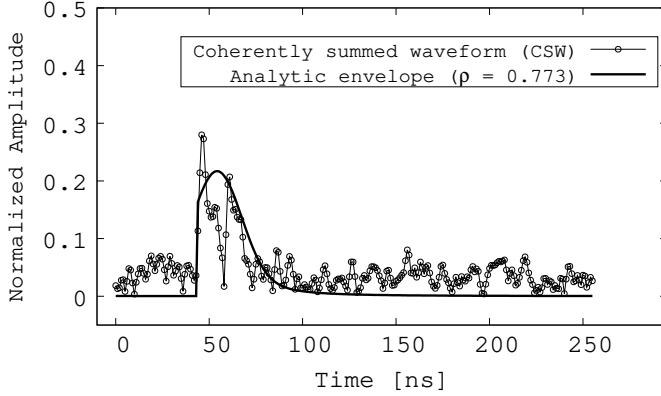

FIG. 7: A direct and reflected CSW signal (black dots and thin black line) from a 100 PeV UHE-ν, matched to an analytic envelope (thick black line) with a correlation coefficient $\rho = 0.773$.

V. CONCLUSION

The conclusion.

Appendix A: Details

The details.

[1] The IceCube Collaboration, Science **342**, 1242856 (2013), ISSN 0036-8075, 1311.5238.

[2] The IceCube Collaboration, Physical Review Letters **111**, 021103 (2013), ISSN 0031-9007, 1304.5356.

[3] The IceCube Collaboration, The Astrophysical Journal **833**, 3 (2016), ISSN 0004-637X, 1607.08006.

[4] The IceCube Collaboration, Science **361**, 147 (2018), ISSN 0036-8075, 1807.08794.

[5] The IceCube Collaboration, Nature **591**, 220 (2021), ISSN 0028-0836, 2110.15051.

[6] The IceCube Collaboration, Science **378**, 538 (2022), ISSN 0036-8075.

[7] The IceCube Collaboration, Science **380**, 1338 (2023), ISSN 0036-8075.

[8] The KM3NeT Collaboration, Nature **638**, 376 (2025), ISSN 0028-0836.

[9] The IceCube Collaboration, Physical Review D **98**, 062003 (2018), ISSN 2470-0010, 1807.01820.

[10] The IceCube-Gen2 Collaboration, arXiv (2020), 2008.04323.

[11] J. C. Hanson and R. Hartig, Phys. Rev. D **105**, 123019 (2022), URL https://link.aps.org/doi/10.1103/PhysRevD.105.123019.

[12] J. C. Hanson and A. L. Connolly, Astroparticle Physics **91**, 75 (2017), ISSN 0927-6505.

[13] J. Alvarez-Muniz, P. M. Hansen, A. Romero-Wolf, and E. Zas, Phys. Rev. D **101**, 083005 (2020), URL https://link.aps.org/doi/10.1103/PhysRevD.101.083005.

[14] J. C. Hanson et al, Astroparticle Physics **62**, 139 (2015), ISSN 0927-6505, 1406.0820.

[15] J. C. Hanson et al, Journal of Glaciology **61**, 438 (2015), ISSN 0022-1430.

[16] J. Avva, J. Kovac, C. Miki, D. Saltzberg, and A. Vieregg, Journal of Glaciology (2014), 1409.5413.

[17] D. Saltzberg, P. Gorham, D. Walz, C. Field, R. Iverson, A. Odian, G. Resch, P. Schoessow, and D. Williams, Physical review letters **86**, 2802 (2001), ISSN 0031-9007.

[18] P. Miocinovic, R. Field, P. Gorham, E. Guillian, R. Milincic, D. Saltzberg, D. Walz, and D. Williams, Physical Review D **74**, 043002 (2006), ISSN 2470-0029, hep-ex/0602043.

[19] P. W. Gorham, S. W. Barwick, J. J. Beatty, D. Z. Besson, W. R. Binns, C. Chen, P. Chen, J. M. Clem, A. Connolly, P. F. Dowkontt, et al. (ANITA Collaboration), Phys. Rev. Lett. **99**, 171101 (2007), URL https://link.aps.org/doi/10.1103/PhysRevLett.99.171101.

[20] C. Glaser et al, The European Physical Journal C **80**, 77 (2020), ISSN 1434-6044, 1906.01670.

[21] The ARIANNA Collaboration, Journal of Cosmology and Astroparticle Physics **2018** (2018).

[22] The ARA Collaboration, Astroparticle Physics **108**, 63 (2019), ISSN 0927-6505, URL `https://www.sciencedirect.com/science/article/pii/S0927650518301154`.

[23] The ARIANNA Collaboration, Journal of Instrumentation **15**, P09039 (2020), 2006.03027.

[24] C. Deaconu, A. G. Vieregg, S. A. Wissel, J. Bowen, S. Chipman, A. Gupta, C. Miki, R. J. Nichol, and D. Saltzberg, Physical Review D **98**, 043010 (2018), ISSN 2470-0010, 1805.12576.

[25] C. Welling and T. R.-G. Collaboration, The Cryosphere **18**, 3433 (2024).

[26] R. V. Buniy and J. P. Ralston, Physical Review D **65** (2001), ISSN 2470-0029.

[27] E. Zas, F. Halzen, and T. Stanev, Physical Review D **45**, 362 (1992).

[28] DLMF, *NIST Digital Library of Mathematical Functions*, http://dlmf.nist.gov/, Release 1.1.1 of 2021-03-15, f. W. J. Olver, A. B. Olde Daalhuis, D. W. Lozier, B. I. Schneider, R. F. Boisvert, C. W. Clark, B. R. Miller, B. V. Saunders, H. S. Cohl, and M. A. McClain, eds., URL `http://dlmf.nist.gov/`.

[29] G. B. Rybicki, Computers in Physics **3**, 85 (1989), ISSN 0894-1866.

[30] I. Kravchenko et al, Physical Review D **85**, 062004 (2012), ISSN 2470-0029, 1106.1164.

[31] J. A. Aguilar, P. Allison, J. J. Beatty, H. Bernhoff, D. Besson, N. Bingefors, O. Botner, S. Buitink, K. Carter, B. A. Clark, et al., Journal of Instrumentation **16**, P03025 (2021), 2010.12279.

[32] J. Alvarez-Muniz, A. Romero-Wolf, and E. Zas, Physical Review D **84**, 103003 (2011), ISSN 2470-0029, 1106.6283.

[33] A. Anker, S. Barwick, H. Bernhoff, D. Besson, N. Bingefors, D. García-Fernández, G. Gaswint, C. Glaser, A. Hallgren, J. Hanson, et al., Journal of Cosmology and Astroparticle Physics **2019**, 030 (2019), 1909.02677.